

Article

# Improved Instruments and Methods for the Photographic Study of Spark-Induced Cavitation Bubbles

Qi Zhang , Jing Luo <sup>\*</sup>, Yanwei Zhai and Yilan Li

State Key Laboratory of Hydraulics and Mountain River Engineering, Sichuan University, Chengdu 610065, China; scu\_zq@163.com (Q.Z.); zhaiyw1992@163.com (Y.Z.); yilan\_li\_c@163.com (Y.L.)

\* Correspondence: luojing@scu.edu.cn; Tel.: +86-138-8052-7265

Received: 27 September 2018; Accepted: 15 November 2018; Published: 18 November 2018



**Abstract:** An underwater spark is able to induce a cavitation bubble, and this principle has been utilized to make cavitation bubble generators for several decades. In this paper, an improved instrument for generating spark-induced cavitation bubbles is described in detail. The voltage time history inside the instrument is measured to show the working process and principle. Cavitation bubbles are generated by the instrument and recorded by a high-speed camera. The radius time history of the bubble is obtained using an image processing algorithm. The ratio of its minimum radius to its maximum radius reaches ~0.2, which indicates that there is little undissolved gas in the bubble. With the radius time history, the velocity fields around the bubbles were calculated by the 1D continuity flow equation, and the pressure fields were calculated by the 1D Euler equation. One cavitation bubble is chosen and discussed in detail. The velocity and pressure on the bubble interface achieve their maximums (~25 m/s and ~1.2 MPa, respectively) at the same time, when the radius is at its minimum (~1 mm). Some statistical results are also presented to show the effect of the instrument.

**Keywords:** bubble dynamics; cavitation; high-speed camera; oscillating bubble; Rayleigh-Plesset equation; spark-induced bubble

## 1. Introduction

The spark, laser and ultrasound methods are common methods for inducing cavitation bubbles in still water in order to study the mechanism of cavitation and cavitation erosion. The spark method is widely used to study a single cavitation bubble or the interaction between cavitation bubbles.

As early as 1952, the spark method was used to induce a single cavitation bubble in still water in order to overcome the difficulties in the pressure measurement of cavitation bubbles in flowing water. Cavitation bubbles induced by a Venturi nozzle and a spark generator were recorded by a high-speed camera, with a frame rate of 8000 fps. Harrison found that two kinds of bubbles had similar behavior [1]. The pressure near a spark-induced bubble was measured by a pressure transducer and recorded by an oscilloscope.

From then on, the spark method was used in many papers on the mechanism of cavitation erosion [2–7].

Until 1975, Lauterborn and Bolle generated a single cavitation bubble with a laser pulse [8]. The laser pulse substituted spark in some fields [9–14].

Compared with the laser-induced bubble, the spark-induced bubble has some disadvantages. For example, the electrodes affect the motion of bubbles, there is more undissolved gas after the

spark-induced bubble collapses, and the undissolved gas limits the power of cavitation bubble collapse [9,13,15–17].

After either laser- or spark-induced cavitation bubbles collapse, there are undissolved gases. The main component of the gases may be hydrogen produced by the plasma [18].

In spite of these disadvantages, sparks are more convenient in generating several cavitation bubbles to study the interaction between them. In addition, the power of sparks has a wider range. As a result, it is more convenient to generate cavitation bubbles with varying radii.

Therefore, a spark device is utilized to study the interaction of cavitation bubbles with a phase difference [19,20], the interaction between cavitation bubbles and rigid particles [21–24], the interaction between cavitation bubbles and a free surface [25–28], and the interaction between cavitation bubbles and air bubbles [29–31].

Sparks cannot be substituted by lasers in these fields, while the existing research focuses more on cavitation bubbles and less on the devices. It is essential to overcome the disadvantages and improve the device.

A low-voltage device was introduced by Goh et al. [32]. This device is able to accurately generate cavitation bubbles with various radii by adjusting the length of its electrodes. The rated voltage of the device is 60 V, which is relatively safe and causes less electromagnetic interference, compared with other electronic equipment. However, the bubbles induced by the low-voltage device contain a lot of undissolved gas.

In order to reduce the amount of undissolved gas, in this paper a high-voltage instrument was designed and built to generate spark-induced cavitation bubbles. The voltage across a capacity in the instrument was measured to show the charging and discharging process. Cavitation bubbles were generated and recorded to test the instrument.

## 2. Materials and Methods

The core of the experiment system is the spark instrument. The spark instrument consists of a transformer, silicon stack, capacitor, resistors, a pair of hemispheres, a pair of needle electrodes and a water tank, as shown in Figure 1. A 220 V 50 Hz power supply and a push button switch are connected to the input of the transformer. A 50 kV 0.25  $\mu$ F capacitor and a silicon stack are connected to the 20-kV output of the transformer. Across the capacitor, there are two more circuits. On one of them, a variable resistor, a pair of hemispheres and a pair of needle electrodes are connected in a series. Sparks are generated between hemispheres and between needle electrodes at the same time. On the other circuit, across the capacitor, a 1 M $\Omega$  resistor and a 1 k $\Omega$  resistor are connected in a series for voltage measurement.

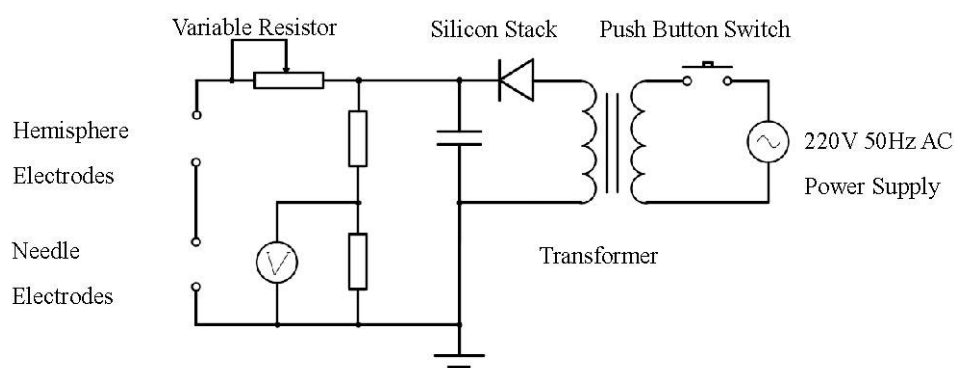


**Figure 1.** A circuit diagram of the spark instrument.

As shown in Figure 2, a transformer, silicon stack and capacitor are placed on a metal plate, which is connected to the ground. The transformer is also connected to a power supply. The push button switch on the power wire is not shown in Figure 2. The bar resistor crosses and connects the capacitor

and the hemisphere. There are some wiretaps on the top of the bar resistor. By shorting out the taps, the resistance can be changed to  $200\ \Omega$ ,  $300\ \Omega$ ,  $400\ \Omega$ ,  $500\ \Omega$  or  $600\ \Omega$ . The resistor was designed to limit the currency in the circuit for safety. It can also be used to control the size of the cavitation bubble, especially when some operating liquids with low heat capacity (e.g., glycerol) are used. In our case, the resistance was maintained at  $200\ \Omega$  to generate a relatively large cavitation bubble. The hemispheres are sealed in a glassy shell. The distance between the hemispheres is adjustable. The needle electrodes are under the hemispheres and in the water tank. They are tungsten needles, with a diameter of 1 mm.

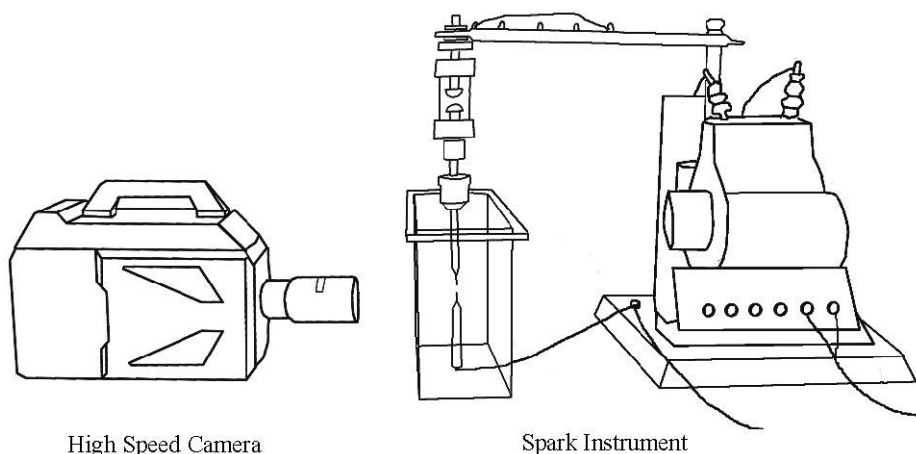


**Figure 2.** A line drawing of the high-speed camera and the experimental system.

When the button, mentioned above, is pushed, the instrument starts working. The transformer increases the voltage dozens of times. The silicon stack converts the alternating current into a direct current. The capacitor is charged until the gaps break and sparks are produced. The spark in the water induces the cavitation bubble.

The voltage across the capacitor exactly describes the process. It was recorded by a data acquisition device (DAQ) with a sampling frequency of 100,000 samples per second and a resolution of 16 bits.

As shown in Figure 3, at times a and c, the button switch was pushed and released, respectively. While the switch is on (time b), the gaps between hemispheres and between needles broke, and the voltage sharply dropped to 0. After time b, the capacitor was recharged, since the switch was still on.

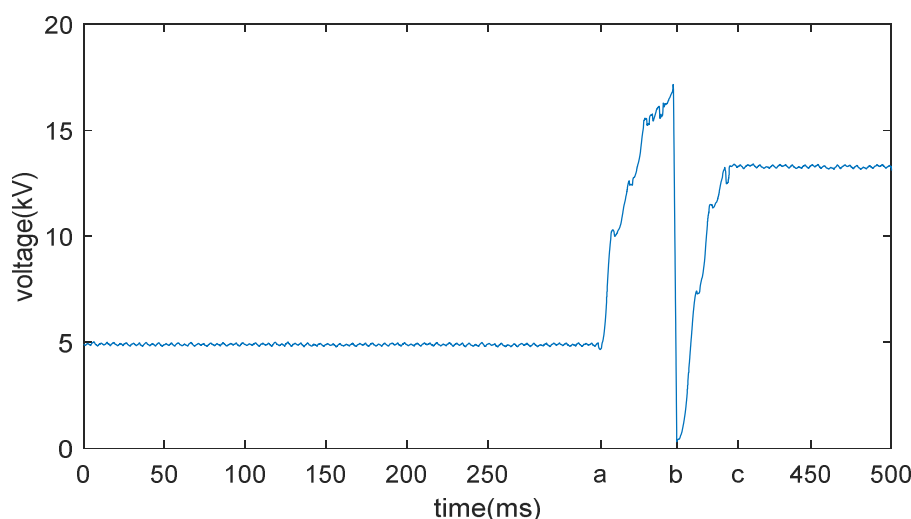


**Figure 3.** Time history of the voltage across the capacitor.

The lifetime of the spark is dozens of microseconds, while the lifetime of the spark-induced cavitation bubble is about several hundred microseconds. These short processes were recorded by a Photron Fastcam SA-Z high-speed camera, with a frame rate of 100,000 fps, in our experiment. To make the edge of the cavitation bubble smooth and sharp, the illumination of the experiment was meticulously designed. A uniform large bulb with a hood was used. The bulb was fixed on an elevator-shelf. The center of the lens, cavitation bubble and bulb formed a line. The bulb was on the right of the water tank and is not shown in Figure 2.

The breakdown voltage at time b in Figure 3 can be changed by adjusting the distance between hemisphere electrodes. The breakdown voltage affects the radius of the cavitation bubble.

The environmental conditions are listed in Table 1. The data were reported by the China Meteorological Administration. The water used in our experiment was deionized, in which the dissolved gas was saturated.

**Table 1.** Environmental conditions.

Day Average Temperature (°C)	Atmospheric Pressure (kPa)	Humidity (%)
5.6	96.7	93

### 3. Results

#### 3.1. Photos

Some photos are shown in Figure 4. The recording rate is 100,000 fps, and the shutter speed is 8.39  $\mu$ s. The cavitation bubble is induced soon after the spark appears. Then, the bubble explodes and collapses periodically. In this paper, the first two cycles are studied.

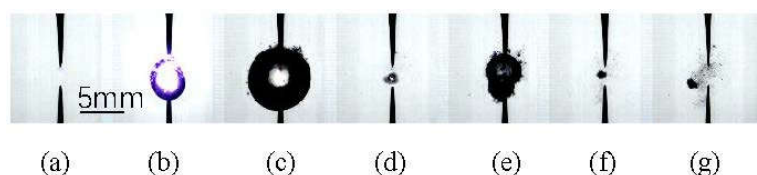


**Figure 4.** A spark-induced cavitation bubble at different stages, where the record rate is 100,000 fps, and the shutter speed is 8.39  $\mu$ s. (a)  $t = 0 \mu$ s, a spark appears; (b)  $t = 100 \mu$ s, the plasma is glowing, and the cavitation bubble is exploding; (c)  $t = 500 \mu$ s, the cavitation bubble explodes at the maximum; (d)  $t = 950 \mu$ s, the cavitation bubble collapses at the minimum; (e)  $t = 1230 \mu$ s, the cavitation bubble rebounds at the maximum; (f)  $t = 1480 \mu$ s, the cavitation bubble collapses at the minimum again; (g)  $t = 2700 \mu$ s, the undissolved gas, after several explode–collapse cycles.

Note the minimum size in Figure 4d. The primary goal of our work is to reduce the size in order to achieve a high impact pressure. At the moment, the kinetic energy of the water had been transferred into the pressure potential energy of the gas, if the dissipation is neglected. The smaller the amount of gas, the larger the pressure.

If the cavitation bubble is approximated into a sphere, the radius will be enough to describe its size. To estimate the radius, an image processing algorithm is designed in our paper.

### 3.2. Image Processing Algorithm

The first step is binarizing, namely, turning the photos into black and white, with a global threshold. The threshold is just the median of the grayscales of all the pixels. Alternatively, the threshold can be determined by the algorithm proposed by Bradley [33]. This algorithm calculates local adaptive thresholds, rather than a global one. After binarizing, a binary matrix is obtained, where 0 and 1 stand for black and white, respectively. The second step is taking an image, with only the needle electrodes as a template, and removing it from the image with both electrodes and the bubble. Then, a median filter, a smoothing filter and a filling algorithm are applied successively. Finally, the number of white pixels are counted, and the area is calculated with the area of a single pixel. All of the intermediate and final results of a large bubble and a small bubble are shown in Figure 5. The same algorithm and parameters were applied to the bubbles.

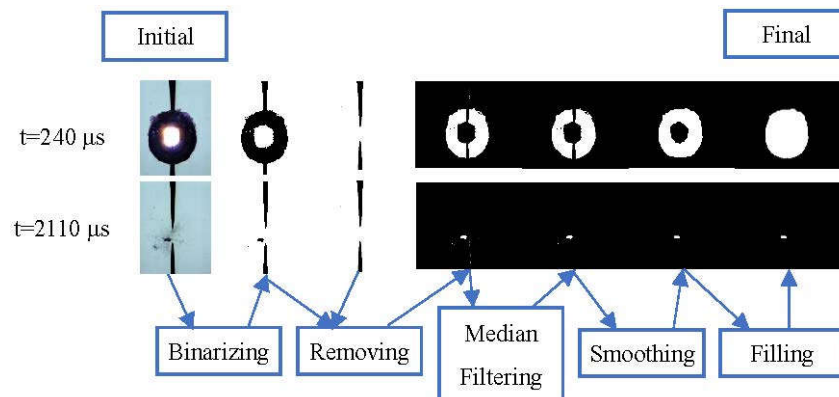


**Figure 5.** Flow chart, intermediate results and the final result of the image processing algorithm.

The white area in Figure 5 is the projected area of the bubble  $S$ :

$$S = \pi R_B^2 \quad (1)$$

where  $R_B$  is the equivalent radius of the bubble.

The error of the equivalent radius  $R_B$  has two main sources. First, the algorithm may treat the edge of the bubble in the wrong way, especially when the edge is rough or blurred. In order to estimate the value of the error, a series of cavitation bubbles were measured manually. The area of the bubble was marked manually. The pixels of the marked area were counted by software. The radius was also calculated by Equation (1). The radii, measured manually, were compared with those measured by the image processing algorithm. As a result, the maximum error is 1.0 pixel. The maximum relative error is 1.3%. Second, the size of the pixel was measured by a transparent ruler, with an accuracy of 1 mm. The width of the photo is 384 pixels and 17.4 mm. The size of a pixel is  $0.045 \pm 0.003$  mm. The relative error is 5.7%. As the two kinds of error are independent, the total relative error of the radius is the sum of them, namely, 7.0%.

### 3.3. Radius Time History

The radius in each frame is calculated with the method mentioned above. The time history is plotted in Figure 6. In the initial stage, the points before 0.14 ms are missing, because the spark is too bright, and the photos are overexposed. The radii of the two cycles are fitted with quadratic functions. The functions will act as a boundary condition, as shown below.

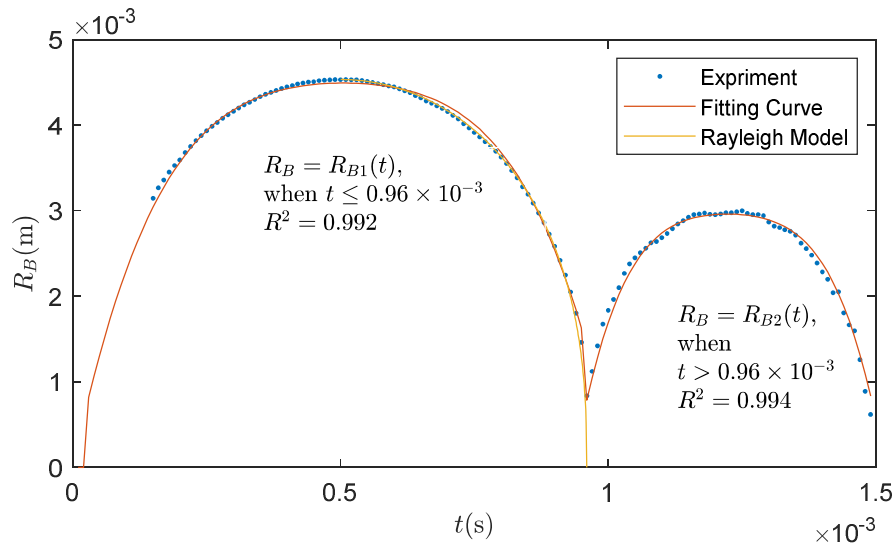


**Figure 6.** Radius time history of the cavitation bubble in the first two cycles.

### 3.4. Breakdown Voltage and Bubble Radius

The breakdown voltage is not quite stable because the spark discharge is a random process. It is affected by the air condition, that is, dust, humidity and temperature. To reduce the influence of the environment, the hemisphere electrodes are sealed in a glassy shell. The breakdown voltage can be changed roughly by adjusting the distance between hemisphere electrodes.

The breakdown voltage affects the size of the cavitation bubble. The relationship is shown in Figure 7, where  $d$  stands for the distance between two hemisphere electrodes. The cavitation bubbles, obtained with the same parameter, were still quite different because of the randomness. The problem is difficult to overcome, because almost no electrical component can stand dozens of kilovolts to substitute the air gap.

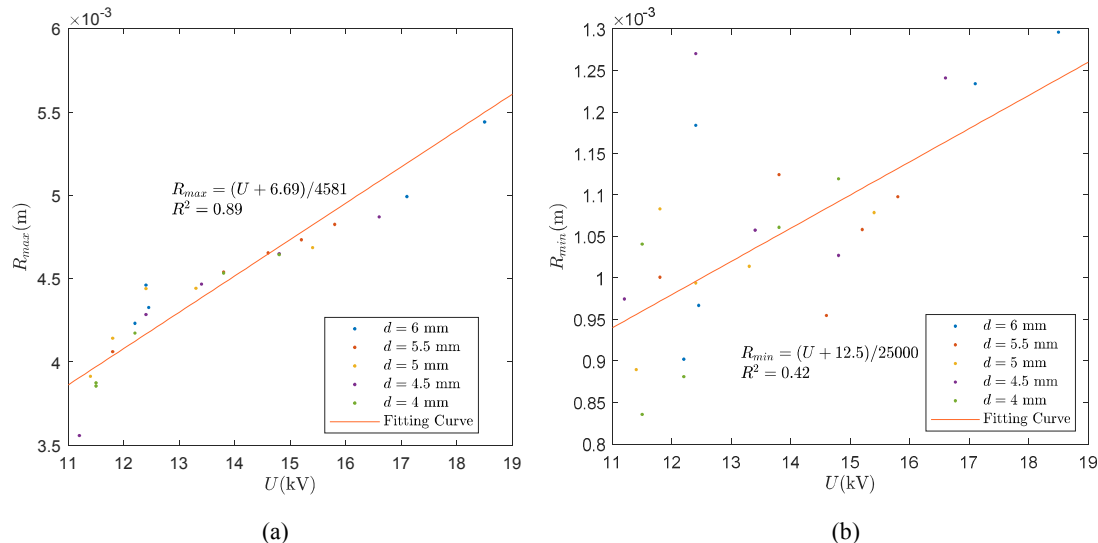


**Figure 7.** Relationship between breakdown voltage and the radius of cavitation bubbles.  
**(a)** The relationship between breakdown voltage and maximum radius of the cavitation bubbles;  
**(b)** the relationship between breakdown voltage and minimum radius of the cavitation bubbles.

The relationship between the breakdown voltage and the maximum radius of the cavitation bubble is obviously positive, which means that a larger breakdown voltage leads to a larger

bubble. The relationship between the breakdown voltage and the minimum radius does not have a clear correlation.

#### 4. Discussion

##### 4.1. Single Bubble Dynamics

We have assumed that the cavitation bubble is spherical. Thus, the motion of the fluid around the bubble can be described with the 1D continuity equation:

$$\frac{\partial(r^2 v_r)}{\partial r} = 0 \quad (2)$$

Regardless of viscosity and compressibility, the pressure can be solved by the 1D Euler Equation:

$$\frac{\partial v_r}{\partial t} + v_r \frac{\partial v_r}{\partial r} = -\frac{1}{\rho} \frac{\partial P}{\partial r} \quad (3)$$

In Equation (2),  $v_r$  can be solved by the separation variable method, as follows:

$$v_r(r, t) = R(r)T(t) \quad (4)$$

Hence,

$$\frac{\partial R(r)}{\partial r} = 0 \quad (5)$$

Therefore,

$$R(r) = \frac{C}{r^2} \quad (6)$$

$T(t)$  is completely determined by the boundary conditions. Therefore,

$$v_r = \frac{T(t)}{r^2} \quad (7)$$

Replacing the above equation with Equation (2) gives

$$\frac{1}{r^2} \frac{dT(t)}{dt} - 2 \frac{T(t)}{r^5} = -\frac{1}{\rho} \frac{\partial P}{\partial r} \quad (8)$$

This gives

$$P = \frac{\rho}{r} \frac{dT(t)}{dt} - 8\rho \frac{T(t)}{r^4} + C \quad (9)$$

At infinity, the pressure is zero. So, the integral constant  $C$  is equal to zero.

If the function  $T(t)$  is solved with the boundary condition, then the velocity field  $v_r$  and the pressure field  $P$  will be obtained.

We treat the motion of the cavitation bubble as a known condition and then calculate the pressures that motivate the motion.

The velocity at the cavitation bubble surface is

$$v_r|_{r=R_B} = dR_B/dt \quad (10)$$

where  $R_B$  is the radius of the cavitation bubble.

According to Equation (7),  $v_r|_{r=R_B} = T(t)/(R_B^2)$ . Therefore,

$$\frac{T(t)}{R_B^2} = \frac{dR_B}{dt} \quad (11)$$

which gives

$$T(t) = R_B^2 \frac{dR_B}{dt} \quad (12)$$

Replacing Equation (12) with Equation (7) gives

$$v_r = \frac{R_B^2}{r^2} \frac{dR_B}{dt} \quad (13)$$

This is the same as that in the Rayleigh–Plesset equation.

Replacing Equation (12) with Equation (9),

$$P = \frac{\rho}{r} \left( 2R_B \left( \frac{dR_B}{dt} \right)^2 + R_B^2 \frac{d^2 R_B}{dt^2} \right) - 8\rho \frac{R_B^2}{r^4} \frac{dR_B}{dt} \quad (14)$$

Now, we use the Taylor series to approximate  $R_B(t)$ . The Taylor series for  $R_B(t)$  at  $t = t_0$  is

$$R_B(0) + R_B^{(1)}(0)(t - t_0) + \frac{R_B^{(2)}(0)}{2!}(t - t_0)^2 + \frac{R_B^{(3)}(0)}{3!}(t - t_0)^3 + \frac{R_B^{(4)}(0)}{4!}(t - t_0)^4 + o(t) \quad (15)$$

We omit the high-order terms and keep the first four order terms:

$$R_B(t) = a_0 + a_1 t + a_2 t^2 + a_3 t^3 + a_4 t^4 \quad (16)$$

where  $a_0, \dots, a_4$  are constant factors.

Note that the function  $R_B(t)$  is not continuous, and it breaks when the bubble collapses at the minimum. Thus,  $R_B(t)$  is a piecewise function. By fitting the experimental data, the factors at the local coordinates are obtained, as shown in Table 2.

**Table 2.** Factors in the polynomial function.

	$a_0$	$a_1$	$a_2$	$a_3$	$a_4$
$R_{B1}(t)$	$-9.4 \times 10^{-6}$	$1.1 \times 10^{-5}$	$-1.1 \times 10^{-2}$	$5.8 \times 10^{-4}$	$9.0 \times 10^1$
$R_{B2}(t)$	$-5.9 \times 10^{-5}$	$-2.0 \times 10^{-4}$	$-2.0 \times 10^{-2}$	$-5.0 \times 10^{-2}$	$5.9 \times 10^1$

Velocity field  $v_r(r, t)$  and pressure field  $P(r, t)$  can be solved by replacing the factors in the formulas, shown above. In our paper, this process is conducted by mathematical software.

The calculated velocity field and pressure field are plotted as contour maps, as shown in Figure 8.

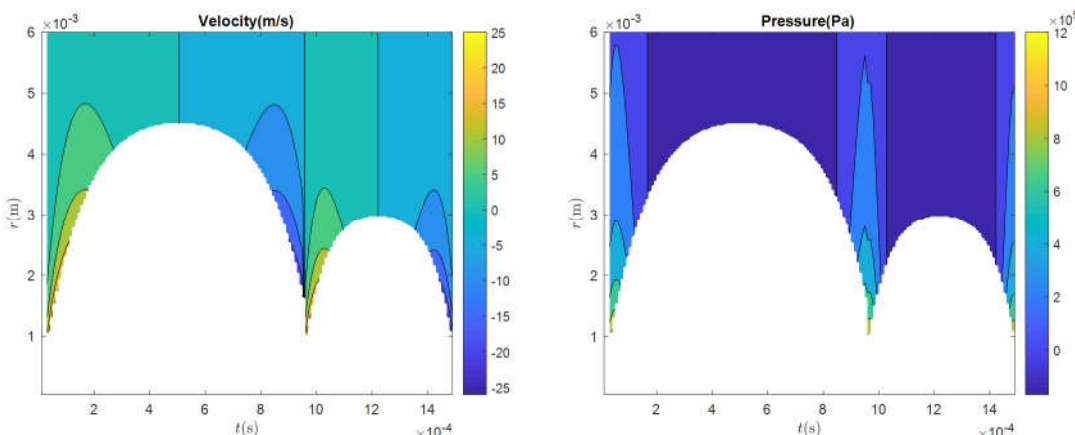


**Figure 8.** The velocity and pressure contour maps, obtained by the analytical method.

When the cavitation bubble collapses, the velocity and pressure reach over 20 m/s and 1.2 MPa, respectively.

Both our model and the Rayleigh model assume that the bubble is a sphere. Compared with the Rayleigh model, our model provides a practical way to estimate the maximum pressure when the cavitation bubble collapses. The Rayleigh model assumes that there is no residual gas after collapse. Thus, the impact pressure is theoretically infinite. The Rayleigh model fits the experimental results very well when the bubble is large. However, when the bubble becomes small, the Rayleigh model predicts a larger radius rate over time.

#### 4.2. Statistical Properties

The process above was repeated 25 times in our experiment. The maximum radius  $R_{max}$ , the minimum radius  $R_{min}$ , the time of the 1st collapse  $T_c$  and the maximum pressure after the first collapse are recorded for each time.

The maximum radius  $R_{max}$  and the collapse time  $T_c$  have an obvious linear correlation, where  $R^2 = 0.98$ , as shown in Figure 9a. Moreover, the correlation between  $R_{max}$  and  $T_c$  can be calculated with the Rayleigh–Plesset equation, as follows:

$$T_c = 0.915 \left( \frac{\rho_L R_{max}^2}{p_\infty - p_v} \right)^{\frac{1}{2}} \quad (17)$$

where  $\rho_L$  is the density of water. If  $\rho_L$ ,  $p_\infty$  and  $p_v$  are constant, the correlation between  $T_c$  and  $R_{max}$  will be linear. The saturated vapor pressure  $p_v$  was treated as an unknown variable, because the spark-induced cavitation is not a simple isothermal process. It was fitted with the experimental data. The fitting result was 23,299 Pa, which can be considered an equivalent value, at 64 °C. This means that the bubbles generated by the instrument have a similar behavior as those induced by the pressure difference at 64 °C.

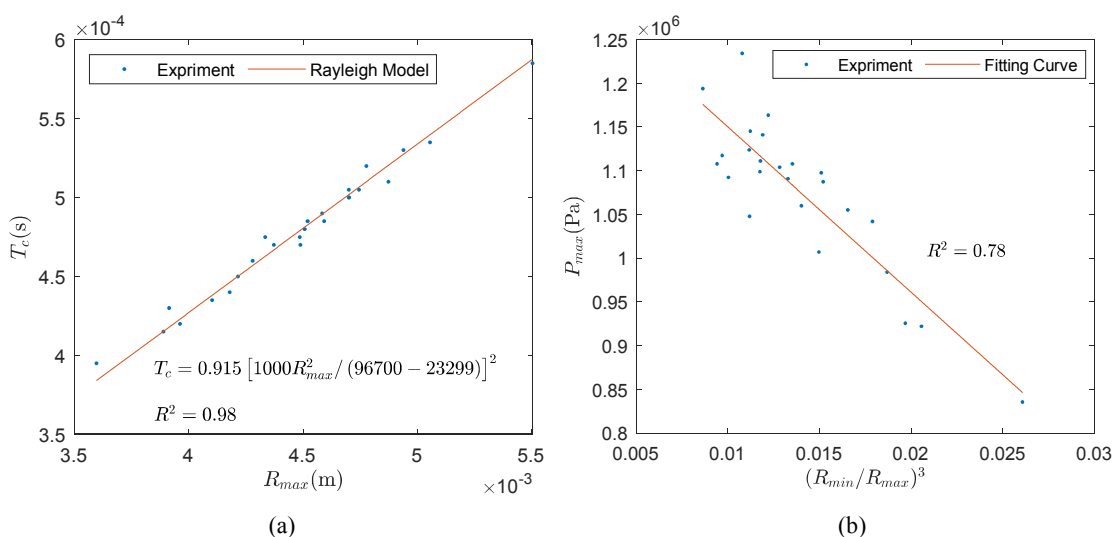


**Figure 9.** The statistical correlation of cavitation bubbles. (a) The correlation between the maximum radius and the period; (b) the correlation between the maximum pressure and the volume ratio.

The volume ratio  $(R_{min}/R_{max})^3$  and maximum pressure  $P_{max}$  have a negative correlation, as shown in Figure 9b. Reducing the ratio is crucial for obtaining a high impact pressure. Unfortunately, the ratio depends strongly on the nature of the heat source. Generally, the laser-induced bubble has less undissolved gas and a higher volume ratio of  $(R_{min}/R_{max})^3$  [18]. Among our spark-induced bubbles, the minimum of the volume ratios is 0.008, as shown in Figure 9b. This is small compared with other spark-induced cavitation bubbles [18,29,32], but still larger than those induced by laser.

The relationship between  $(R_{min}/R_{max})^3$  and  $P_{max}$  is not strong, because the data are dispersed. The error mainly comes from the process of the curve fitting of the radius time history.

How the breakdown voltage affected the maximum pressure of the cavitation bubble was also investigated. As shown in Figure 10, the correlation is weak, as the dots are quite scattered. The main reason for this is that the maximum pressure depends on both the maximum and minimum radius. As mentioned in the last section, the minimum radius also has a poor correlation with the breakdown voltage. As a result, it is currently impossible to generate a certain impact pressure by adjusting the parameter of the instrument.

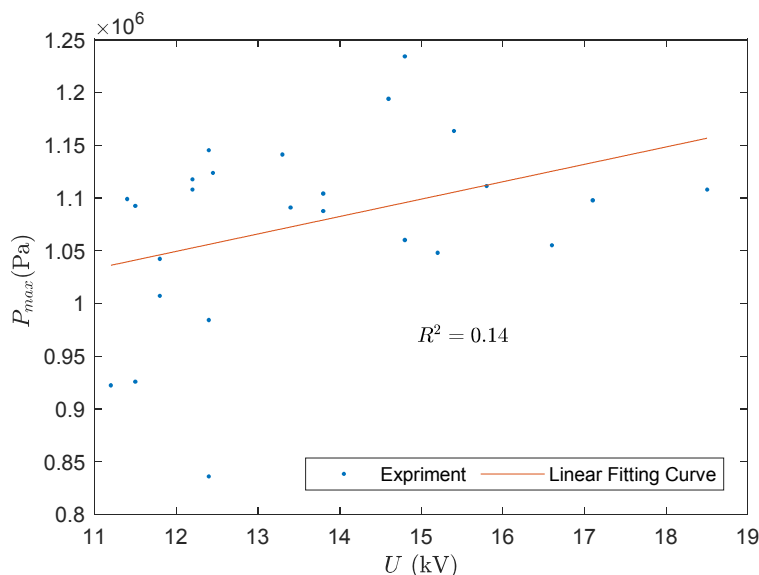


**Figure 10.** The relationship between the breakdown voltage and maximum pressure.

## 5. Conclusions

In this paper a spark instrument is designed to induce cavitation bubbles. The voltage inside shows the charge and discharge processes clearly and exactly. Additionally, an image process algorithm is promoted to calculate the radius of the cavitation bubbles.

The time history of the cavitation bubble fits the Rayleigh model very well. This means that the bubbles have a similar behavior as those induced by the pressure difference. The cavitation bubbles induced by our instrument contain little undissolved gas. The theoretical analysis and experimental data show that the volume of undissolved gas and the maximum impact pressure have a negative correlation. In our experiment, the ratio of the minimum radius to the maximum radius reaches 0.2. Thus, the impact pressure during collapse reaches 1.2 MPa.

The main shortcoming of the instrument is the randomness of the spark discharge. The cavitation bubbles induced by the same experimental conditions can be quite different. The size of the cavitation bubble can be changed roughly by adjusting the distance between the two hemisphere electrodes.

In short, the instrument utilizes a high voltage to induce cavitation bubbles, with little undissolved gas. As a necessary cost, the size of the cavitation bubble becomes almost uncontrollable.

**Author Contributions:** Conceptualization, Q.Z. and Y.Z.; data curation, Q.Z.; formal analysis, Q.Z.; funding acquisition, J.L.; investigation, Q.Z.; methodology, Q.Z.; project administration, J.L.; resources, J.L.; software, Q.Z. and J.L.; supervision, J.L.; validation, Q.Z., Y.Z. and Y.L.; visualization, Q.Z.; writing—original draft, Q.Z.; writing—review & editing, Q.Z. and J.L.

**Funding:** This research was funded by the National Basic Research Development Program of China, grant number 2013CB035905, the National Natural Science Foundation of China, grant number 51409180, and the Postdoctoral R&D Program of Sichuan University, grant number 2018SCU12061.

**Conflicts of Interest:** The authors declare no conflict of interest.

## References

1. Harrison, M. An Experimental Study of Single Bubble Cavitation Noise. *J. Acoust. Soc. Am.* **1952**, *24*, 776–782. [[CrossRef](#)]
2. Shutler, N.D.; Mesler, R.B. A Photographic Study of the Dynamics and Damage Capabilities of Bubbles Collapsing Near Solid Boundaries. *J. Basic Eng.* **1965**, *87*, 511–517. [[CrossRef](#)]
3. Shima, A.; Takayama, K.; Tomita, Y.; Ohsawa, N. Mechanism of impact pressure generation from spark-generated bubble collapse near a wall. *AIAA J.* **1983**, *21*, 55–59. [[CrossRef](#)]
4. Ward, B.; Emmony, D.C. Direct observation of the pressure developed in a liquid during cavitation-bubble collapse. *Appl. Phys. Lett.* **1991**, *59*, 2228–2230. [[CrossRef](#)]
5. Luo, J.; Xu, W.; Deng, J.; Zhai, Y.; Zhang, Q.; Luo, J.; Xu, W.; Deng, J.; Zhai, Y.; Zhang, Q. Experimental Study on the Impact Characteristics of Cavitation Bubble Collapse on a Wall. *Water* **2018**, *10*, 1262. [[CrossRef](#)]
6. Jayaprakash, A.; Hsiao, C.-T.; Chahine, G. Numerical and Experimental Study of the Interaction of a Spark-Generated Bubble and a Vertical Wall. *J. Fluids Eng.* **2012**, *134*, 031301. [[CrossRef](#)]
7. Ma, X.; Huang, B.; Zhao, X.; Wang, Y.; Chang, Q.; Qiu, S.; Fu, X.; Wang, G. Comparisons of spark-charge bubble dynamics near the elastic and rigid boundaries. *Ultrason. Sonochem.* **2018**, *43*, 80–90. [[CrossRef](#)] [[PubMed](#)]
8. Lauterborn, W.; Bolle, H. Experimental investigations of cavitation-bubble collapse in the neighbourhood of a solid boundary. *J. Fluid Mech.* **1975**, *72*, 391–399. [[CrossRef](#)]
9. Philipp, A.; Lauterborn, W. Cavitation erosion by single laser-produced bubbles. *J. Fluid Mech.* **1998**, *361*, 75–116. [[CrossRef](#)]
10. Lim, K.Y.; Quinto-Su, P.A.; Klaseboer, E.; Khoo, B.C.; Venugopalan, V.; Ohl, C.-D.D. Nonspherical laser-induced cavitation bubbles. *Phys. Rev. E Stat. Nonlinear Soft Matter Phys.* **2010**, *81*, 016308. [[CrossRef](#)] [[PubMed](#)]
11. Vogel, A.; Brujan, E.A.; Schmidt, P.; Nahen, K. Interaction of laser-produced Cavitation bubbles with elastic boundaries. In *IUTAM Symposium on Free Surface Flows; Fluid Mechanics and Its Applications*; Springer: Dordrecht, The Netherlands, 2001; Volume 62, pp. 327–335.
12. Tomita, Y.; Kodama, T. Interaction of laser-induced cavitation bubbles with composite surfaces. *J. Appl. Phys.* **2003**, *94*, 2809–2816. [[CrossRef](#)]
13. Philipp, A.; Lauterborn, W. Damage of Solid Surfaces by Single Laser-Produced Cavitation Bubbles. *Acta Acust. United Acust.* **1997**, *83*, 223–227.
14. Han, B.; Liu, L.; Zhao, X.-T.; Ni, X.-W. Liquid jet formation through the interactions of a laser-induced bubble and a gas bubble. *AIP Adv.* **2017**, *7*, 105305. [[CrossRef](#)]
15. Lindau, O.; Lauterborn, W. Cinematographic observation of the collapse and rebound of a laser-produced cavitation bubble near a wall. *J. Fluid Mech.* **2003**, *479*, 327–348. [[CrossRef](#)]
16. Vogel, A.; Lauterborn, W. Acoustic transient generation by laser-produced cavitation bubbles near solid boundaries. *J. Acoust. Soc. Am.* **1988**, *84*, 719–731. [[CrossRef](#)]
17. Hentschel, W.; Lauterborn, W. Acoustic emission of single laser-produced cavitation bubbles and their dynamics. *Appl. Sci. Res.* **1982**, *38*, 225–230. [[CrossRef](#)]
18. Sato, T.; Tinguely, M.; Oizumi, M.; Farhat, M. Evidence for hydrogen generation in laser- or spark-induced cavitation bubbles. *Appl. Phys. Lett.* **2013**, *102*, 074105. [[CrossRef](#)]
19. Fong, S.W.; Adhikari, D.; Klaseboer, E.; Khoo, B.C. Interactions of multiple spark-generated bubbles with phase differences. *Exp. Fluids* **2009**, *46*, 705–724. [[CrossRef](#)]
20. Luo, J.; Xu, W.; Li, R. High-speed photographic observation of collapse of two cavitation bubbles. *Sci. China Technol. Sci.* **2016**, *59*, 1707–1716. [[CrossRef](#)]
21. Xu, W.; Zhang, Y.; Luo, J.; Zhang, Q.; Zhai, Y. The impact of particles on the collapse characteristics of cavitation bubbles. *Ocean Eng.* **2017**, *131*, 15–24. [[CrossRef](#)]
22. Poulain, S.; Guenoun, G.; Gart, S.; Crowe, W.; Jung, S. Particle motion induced by bubble cavitation. *Phys. Rev. Lett.* **2015**, *114*. [[CrossRef](#)] [[PubMed](#)]
23. Ohl, S.-W.; Wu, D.W.; Klaseboer, E.; Khoo, B.C. Spark bubble interaction with a suspended particle. *J. Phys. Conf. Ser.* **2015**, *656*, 012033. [[CrossRef](#)]
24. Li, S.; Zhang, A.M.; Wang, S.; Han, R. Transient interaction between a particle and an attached bubble with an application to cavitation in silt-laden flow. *Phys. Fluids* **2018**, *30*, 082111. [[CrossRef](#)]

25. Zhang, A.M.; Cui, P.; Wang, Y. Experiments on bubble dynamics between a free surface and a rigid wall. *Exp. Fluids* **2013**, *54*, 1602. [[CrossRef](#)]
26. Cui, P.; Zhang, A.M.; Wang, S.P. Small-charge underwater explosion bubble experiments under various boundary conditions. *Phys. Fluids* **2016**, *28*, 117103. [[CrossRef](#)]
27. Zhang, S.; Wang, S.; Zhang, A.M. Experimental study on the interaction between bubble and free surface using a high-voltage spark generator. *Phys. Fluids* **2016**, *28*, 032109. [[CrossRef](#)]
28. Longuet-Higgins, M.S. Bubbles, breaking waves and hyperbolic jets at a free surface. *J. Fluid Mech.* **1983**, *127*, 103–121. [[CrossRef](#)]
29. Luo, J.; Xu, W.; Niu, Z.; Luo, S.; Zheng, Q. Experimental study of the interaction between the spark-induced cavitation bubble and the air bubble. *J. Hydodyn. Ser. B* **2013**, *25*, 895–902. [[CrossRef](#)]
30. Xu, W.; Bai, L.; Zhang, F. Interaction of a cavitation bubble and an air bubble with a rigid boundary. *J. Hydodyn.* **2010**, *22*, 503–512. [[CrossRef](#)]
31. Kannan, Y.S.; Karri, B.; Sahu, K.C. Letter: Entrapment and interaction of an air bubble with an oscillating cavitation bubble. *Phys. Fluids* **2018**, *30*, 041701. [[CrossRef](#)]
32. Goh, B.H.T.; Oh, Y.D.A.; Klaseboer, E.; Ohl, S.W.; Khoo, B.C. A low-voltage spark-discharge method for generation of consistent oscillating bubbles. *Rev. Sci. Instrum.* **2013**, *84*. [[CrossRef](#)] [[PubMed](#)]
33. Bradley, D.G.R. Adapting Thresholding Using the Integral Image. *J. Gr. Tools* **2018**, *12*, 13–21. [[CrossRef](#)]



© 2018 by the authors. Licensee MDPI, Basel, Switzerland. This article is an open access article distributed under the terms and conditions of the Creative Commons Attribution (CC BY) license (<http://creativecommons.org/licenses/by/4.0/>).